Shape reconstruction of delamination defects using thermographic infrared signals based on an enhanced Canny approach

Almpion Ratsakou, Anastassios Skarlatos, Christophe Reboud, Dominique Lesselier

Version of Record: https://www.sciencedirect.com/science/article/pii/S1350449520305752
Manuscript_d5ee9672053e12f70d8084b3c8b93b6c

Shape reconstruction of delamination defects using thermographic infrared signals based on an enhanced Canny approach

Almpion Ratsakou[a], Anastassios Skarlatos[a], Christophe Reboud[a], Dominique Lesselier[b]

[a] *Université Paris-Saclay, CEA, List, F-91120, Palaiseau, France*
[b] *Université Paris-Saclay, CNRS, CentraleSupélec, Laboratoire des signaux et systèmes, 91190, Gif-sur-Yvette, France*

Abstract

The Canny shape-reconstruction algorithm is combined with the thermographic signal reconstruction (TSR) technique for the characterisation of delamination defects in planar multilayer structures. The adopted approach consists in fitting the raw thermographic images to a low-degree polynomial in the log-log representation of the time axis, according to TSR technique, and then apply the Canny algorithm to the reconstruction of the original signals. The proposed juxtaposition of the two treatments benefits from the inherent signal de-noising and compression of the TSR algorithm, thus enhancing the performance of the overall reconstruction process. The proposed approach has been applied using synthetic signals obtained via a 3D semi-analytical simulation code and the obtained reconstructed images have been compared with the (known) delamination geometry demonstrating satisfactory results.

Keywords: infrared testing, delamination, image reconstruction, Canny algorithm, TSR, semi-analytical solution.

1. Introduction

Infrared non-destructive testing (IR) techniques have received growing attention in recent years thanks to their advantages, that is, fast, high resolution and contactless control, and benefiting from the technological progress in the domain of the hardware, namely infrared cameras and data acquisition equipment. The acquired infrared images are then analysed for the detection and characterization of flaws. Subsurface irregularities will affect the heat diffusion rate leading to a thermal contrast on the surface of the homogeneous work-piece. By analysing alterations or the contrast in the thermal pattern of the material surface, one can obtain information about subsurface flaws.

The material under testing may be heated using various sources as optical excitation, electromagnetic excitation, acoustic excitation, stress excitation. The most common form of active thermography [1] for material evaluation consists in using sources as flash lamps [2] or lasers [3, 4] where a pulse of light instantaneously heats a surface and the resulting temperature change is observed with a thermal camera. This technique is also known as pulsed thermography (PT) [5] or square pulse thermography (SPT) [6] and has been extensively used as inspection technology for composites and layered structures. According to the heating function, other common types of active thermography are stepped thermography (ST) [7], lock-in thermography (LT) [8, 9], pulsed phase thermography (PPT) [10], and frequency modulated thermography (FMT) [11].

The detection of the defects can be on the same side as the heat source or on the opposite side, depending on the type of access to the sample. Typical TNDT procedure results in a sequence of infrared (IR) images, obtained via an IR camera, that reflects the evolution of temperature over time. The recorded thermal response usually is degraded because of several factors. Uneven heating and variations of emissivity on the observed surface are only few of the factors which can cause signal-to-noise-ratio (SNR) problems and limit the potential sensitivity of any method.

Analysing the thermal images may be an intense and not an easy task to perform. The detection and characterization of the defects highly depends on the quality of the images as well as on the techniques used. Signal processing is a crucial mean to extract useful information from raw data captured from sensors. More and more signal processing algorithms including thermographic signal reconstruction (TSR) [12, 13], principal component analysis (PCA) [14], independent component analysis (ICA) [15, 16], wavelet transform [17], Tucker decomposition [18, 19], support vector machine (SVM) [20], and pattern recognition [21] are being used in thermography. The use of any of the aforementioned techniques depends on the physics of the problem and their results are usually qualitative, meaning that the defects are not fully characterised. Depending on the application, the detection and the shape reconstruction of the defects may be a success.

In the present work, the TSR method has been used to reduce the amount of noise in thermal images and local storage requirements while improving the visibility of defects. The technique significantly reduces temporal noise. Even though the TSR is a pixel-based technique, one of its side effects is the reduction of spatial noise, making the images more suitable for the defects' detection.

Underlying defects and discontinuities appear explic-

itly in the reconstructed images with a different intensity. Morphological image processing techniques can be used to detect these abnormalities. Almond *et al.* here [22] suggested the identification procedure called Full Width Half Maximum (FWHM) which is based on the measurement of the distance between the points which correspond to half of the maximum temperature signal. Thermal edge effects for crack-like defects have been calculated using the Wiener-Hopf technique. Lugin and Netzelmann [23] proposed a model–based iterative algorithm for the reconstruction of two– and three–dimensional defect shapes.

More generic image processing techniques can be used for the detection of the defects' edges. A suitable edge–detection technique which can be used for accurate recognition and shape reconstruction is the Canny algorithm [24]. Canny edge detector is a multi-step technique that processes an input image and detects the edges of any objects. Because of its great accuracy, the algorithm is used in computer vision systems, yet not only. In the NDT field the applications of the algorithm are numerous and its usage can be found in several inspection techniques. Alaknanda *et al.* [25] used the Canny algorithm for the flaw detection in radiographic weld images. In a recent work by Yan *et al.* [26] the algorithm has been used for the detection of corrosion via pulse–modulation eddy current inspection. In thermography, Sham *et al.* [27] used the algorithm for the detection of cracks on concrete surfaces heated by a flash lamp.

This paper proposes a new approach for the real–time shape reconstruction of delamination defects in planar multilayer structures based on a combination of the TSR method and the Canny algorithm. To assess the performance of the approach, the proposed algorithm is applied to synthetic thermograms obtained by corrupting simulation results with different levels of additive Gaussian noise.

The numerical simulation of IR procedures involves the solution of the heat conduction problem in the considered work-piece, with and without defects, in order to obtain the temperature distribution at the piece interfaces, which constitutes the measurement. The full solution to this problem can be obtained using a numerical technique like the finite elements method (FEM). Nevertheless, in practical situations it is often meaningful to renounce the detailed information of the complete numerical solution in favour of fast analytical or semi-analytical approximations, which hold the essence of the thermal flow behaviour. A powerful, well-established approach is the so-called thermal quadrupole method, where the original three dimensional problem is approximated as a multilayer one dimensional problem (by ignoring the heat flow in the lateral layers directions) and modelled as a cascade of "quadrupoles" in analogy with the electrical network theory [28, 29, 30].

Should the lateral propagation become no longer negligible, as in the case of thermal image processing at late times considered in this work, the quadrupole approach is not valid anymore, and a more general approach properly accounting for the 3D diffusion should be followed. Semi-analytical formulations are still tractable in this case, provided that the considered geometry consists of canonical pieces and making the assumption that the solution is negligible (or stationary) at sufficient distance from the region of interest. This approach is based on the artificial truncation of the computational domain, referred to in the literature as the truncated region eigenfunction expansion (TREE), and has been successfully applied in electromagnetics for the solution of magnetostatic and low-frequency (eddy-current) problems [31, 32, 33, 34, 35]. Defects can be modelled either directly as part of the geometry like in [33, 34, 35], or indirectly by first applying the TREE method to construct the Green's function accounting for the geometry of the flawless piece and treating the defect as a perturbation by solving the appropriate integral equation [36, 37].

The TREE approach has already been tested for the inversion of thermographic signals in order to estimate the thickness of delamination defects [38]. In this work, this approach is extended to multilayer specimens and is combined with the TSR method for providing the simulated signals to the reconstruction algorithm.

The paper is organised as follows. The considered inspection problem is posed and a semi-analytical solution of the heat conduction problem using the TREE approach is presented in section 2. The defect reconstruction algorithm is then discussed in section 3, where a detailed presentation of the constituting bricks, namely the TSR and the Canny algorithm, is provided. The application of the proposed approach in the case of a two-layer medium embedding a number of delamination patches between the two layers is examined in section 4, and the article is concluded with a brief discussion in section 5.

2. Heat propagation problem in multilayer pieces with delamination defects

2.1. Problem position

Let us consider a planar piece composed of N stacked sheets perfectly joined with another. The medium above and underneath the considered piece is air. The piece is thermally excited at its upper interface by means of an impinging heat flux (flash lamp, laser source, air flow). The exact form of the excitation is irrelevant for the hereafter developed mathematical analysis. Solely its geometrical features, i.e., the shape and the dimensions of the flux spot as well as its intensity, that is, the heat power per unit of surface, are of interest here. We also assume that the considered medium is affected by a delamination flaw located between the ith and the $(i+1)$th layer. As such, it is understood a local loss of contact between the two layers, which physically takes the form of a very thin cavity between the two layers, filled with air. The considered configuration is depicted in Fig. 1.

Each layer i is characterised by its mass density ρ_i, its heat capacity at constant (atmospheric) pressure c_{p_i} and

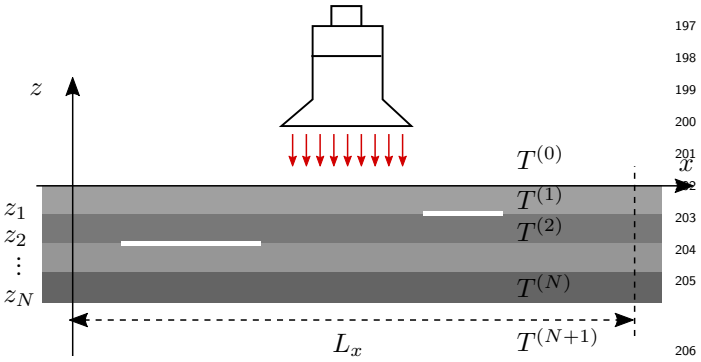

Figure 1: Problem configuration: a planar multilayer medium affected by a number of delamination flaws is thermally excited by an impinging heat flux.

its thermal conductivity, which in the context of this work we assume that it is isotropic κ_i.

We seek to calculate the temperature at every point of the medium throughout an observation time window comprising the excitation and a relaxation time interval after the source switch-off. In particular, we are interested in the temperature distribution at the upper and lower piece-air interface since these distributions are the experimentally accessible information. These two distributions can be extracted by the solution of the associated heat propagation problem, as developed below.

2.2. Formal solution

Let $T^{(i)}(\mathbf{r},t)$ be the temperature distribution inside the ith layer, as shown in Fig. 1, expressed as a function of position $\mathbf{r}$ and time t. Since no heat sources exist inside the layer by hypothesis, $T^{(i)}(\mathbf{r},t)$ satisfies the homogeneous heat equation in this layer

$$\left(\nabla^2 - \frac{1}{\alpha_i}\frac{\partial}{\partial t}\right) T^{(i)}(\mathbf{r},t) = 0, \tag{1}$$

where $\alpha_i = \kappa_i / c_{p_i}\rho_i$ stands for the diffusivity of the layer.

Since we are interested in the transient solution of the heat equation, and we are particularly keen to the early time response, the established (and also most efficient) approach is to consider the problem in Laplace domain. Application of the Laplace transform to (1) yields

$$\left(\nabla^2 - \frac{s}{\alpha_i}\right) T^{(i)}(\mathbf{r},s) = 0, \tag{2}$$

s being the Laplace variable.

In media with flaws the total solution for the temperature field can be decomposed into two terms: the solution for the unperturbed medium under the excitation of the considered heat source, and a perturbation term produced by the interaction of the incoming heat flux with the material flaw. Given that we are dealing with a diffusion problem, the latter contribution can be considered as negligible at sufficiently remote distance from the flaw, in the same way we treat the flaw field in eddy current problems. As a consequence, the temperature field at these distances will be dominated by the solution for the unperturbed medium, which for an infinite planar piece depends solely on the dimensions of the incoming heat flux. Hence, for extended (practically infinite) fluxes, the computational domain can be closed (truncated) by a Neumann boundary condition, which assures zero escaping heat flux from the domain boundaries (otherwise stated, an adiabatic condition).

$$\left.\frac{\partial T^{(i)}}{\partial x}\right|_{x=0} = \left.\frac{\partial T^{(i)}}{\partial x}\right|_{x=L_x} = 0, \tag{3}$$

$$\left.\frac{\partial T^{(i)}}{\partial y}\right|_{y=0} = \left.\frac{\partial T^{(i)}}{\partial y}\right|_{y=L_y} = 0, \tag{4}$$

with the computational domain extending from 0 to L_x in the x direction and from 0 to L_y in the y direction. This condition is in accordance with the physics of the solution. If, instead, the consider source has a finite (with respect to the characteristic dimensions of the problem) support, the domain can be truncated either by a Dirichlet (zero temperature) or Neumann (zero flux) condition, as it is the usual practice with the TREE method[1].

In this work we deliberately choose to work with finite support sources since this case leads to simpler mathematical treatment (absence of a zero-order term). It does not lack practical significance either, since narrow lamp spots and point sources like laser beams are also of interest in real world applications. We thus impose

$$T^{(i)}\Big|_{x=0} = T^{(i)}\Big|_{x=L_x} = 0, \tag{5}$$

$$T^{(i)}\Big|_{y=0} = T^{(i)}\Big|_{y=L_y} = 0. \tag{6}$$

Notice here that re-gauging the temperature field to be zero at the ambient conditions, we can apply the homogeneous Dirichlet condition at the domain boundaries. The formal solution for the temperature field in the ith layer reads as

$$T^{(i)} = \sum_{m=1}^{\infty}\sum_{n=1}^{\infty} C_{mn}^{(i)} e^{\eta_{mn}^{(i)}(z-z_{i-1})} w_{mn}(x,y) + \sum_{m=1}^{\infty}\sum_{n=1}^{\infty} D_{mn}^{(i)} e^{-\eta_{mn}^{(i)}(z-z_i)} w_{mn}(x,y) \tag{7}$$

for $i = 1\ldots,N$, with

$$w_{mn}(x,y) = \sin(\kappa_m x)\sin(\lambda_n y)\,, \tag{8}$$

the discrete eigenvalues κ_m and λ_n being determined by the truncation conditions in the x and y directions (5),(6),

[1] It should be underlined here the difference with the eddy-current problems, where the TREE formulation has been extensively studied. In these problems, the excitation term is always localised around the coil and hence one can use either Dirichlet or Neumann conditions in almost every case. The basic criterion in the final choice is mathematical convenience.

namely,

$$\sin(\kappa_m L_x) = 0, \quad \kappa_m = \frac{m\pi}{L_x}, \quad m = 1\ldots,\infty, \tag{9}$$

$$\sin(\lambda_n L_y) = 0, \quad \lambda_n = \frac{n\pi}{L_y}, \quad n = 1\ldots,\infty, \tag{10}$$

and $\eta_{mn}^{(i)}$ being calculated using the dispersion equation

$$\eta_{mn}^{(i)} = \sqrt{\kappa_m^2 + \lambda_n^2 + \frac{s}{a_i}}. \tag{11}$$

Note that the development coefficients $C_{mn}^{(i)}$ and $D_{mn}^{(i)}$ standing for the upwards and downwards evanescent modes have been normalised with respect to the values of the corresponding exponential terms at the lower z_i and upper z_{i-1} interface, respectively. There are different ways to normalise the modes. The one chosen here assures that all the corresponding exponents are negative, resulting in values lower than one, and thus overflows are avoided.

In the air regions above and underneath the piece, only the terms vanishing to infinity must be kept, reducing the general expansion to the following expressions

$$T^{(0)} = \sum_{m=1}^{\infty}\sum_{n=1}^{\infty} D_{mn}^{(1)} e^{-\eta_{mn}^{(0)} z} w_{mn}(x,y) \tag{12}$$

and

$$T^{(N+1)} = \sum_{m=1}^{\infty}\sum_{n=1}^{\infty} C_{mn}^{(N+1)} e^{\eta_{mn}^{(0)}(z-z_N)} w_{mn}(x,y) \tag{13}$$

for the regions above and below the piece, respectively, with $\eta_{mn}^{(0)} = \sqrt{\kappa_m^2 + \lambda_n^2 + s/a_0}$, a_0 standing for the air diffusivity.

The expansion coefficients in (7) and (12),(13) are determined according to the standard procedure by applying the continuity of the temperature and the normal to the interface heat flux across the piece interfaces.

We treat the problem in two steps. First, the solution for the flawless medium is developed, assuming a perfect thermal contact between all layers. The effect of delamination effects is accounted for in a second step by modification of the temperature continuity at the respective interfaces.

2.3. Equation system for the flawless medium

Considering the interface between the i and the $(i+1)$th layers, these two relations are written as

$$\left[T^{(i)} - T^{(i+1)}\right]_{z=z_i} = 0 \tag{14}$$

and

$$\left[J_n^{(i)} - J_n^{(i+1)}\right]_{z=z_i} = J_e, \tag{15}$$

respectively, with the normal heat flux in the ith layer being given by the Fourier's law

$$J_n^{(i)}(x,y) = -\kappa_i \frac{\partial T^{(i)}}{\partial z}. \tag{16}$$

J_e stands for the incoming flux of the heat source, which for the class of problems which we are dealing admits a non-zero value only at the upper interface, where the thermal excitation is applied. Assuming an impinging beam of constant intensity J_e and of arbitrary support $S(x,y)$, the source term can be developed in terms of the modal functions $w_{mn}(x,y)$ as

$$J_e(x,y) = \sum_{m=1}^{\infty}\sum_{n=1}^{\infty} C_{mn}^{(e)} w_{mn}(x,y)\,, \tag{17}$$

where the development coefficients are given by the integrals

$$C_{mn}^{(e)} = J_e \int_0^{L_x}\int_0^{L_y} S(x,y)\, w_{mn}(x,y)\ \mathrm{d}x\ \mathrm{d}y. \tag{18}$$

The above integrals admit closed form expressions for the most usual shapes such as rectangular and circular.

Substituting (7),(12),(13) and (17) in (14),(15) and weighting with w_{mn} we obtain

$$\begin{aligned} &C_{mn}^{(i)} e^{-\eta_{mn}^{(i)} d_i} + D_{mn}^{(i)} \\ &-C_{mn}^{(i+1)} - D_{mn}^{(i+1)} e^{-\eta_{mn}^{(i+1)} d_{i+1}} = 0 \end{aligned} \tag{19}$$

and

$$\begin{aligned} &-\eta_{mn}^{(i)}\kappa_i \left(C_{mn}^{(i)} e^{-\eta_{mn}^{(i)} d_i} - D_{mn}^{(i)}\right) \\ &\eta_{mn}^{(i+1)}\kappa_{i+1} \left(C_{mn}^{(i+1)} - D_{mn}^{(i+1)} e^{-\eta_{mn}^{(i+1)} d_{i+1}}\right) \\ &= C_{mn}^{(e)}\delta_{i,0}, \end{aligned} \tag{20}$$

where $d_i = z_{i-1} - z_i$ and $\delta_{i,0}$ is the Kronecker delta. Notice that for the first and last interface, $C_{mn}^{(1)}$ and $D_{mn}^{(N+1)}$ vanish.

Since the development basis is infinite, we need to truncate the sums (7),(12) and (13) in order to arrive at a solvable system of equations. We are allowed to do that since the series terms are decreasing for increasing mode numbers m and n. Thus, assuming an exact arithmetic, the error can be made arbitrarily small by judicious choice of the number of modes taken into account. Let N_m and N_n be this number for the modes along the x and y directions. The previous result for the continuity relations at the ith interface can be conveniently represented in a matrix form as follows

$$\mathbf{A}^{(i)}\mathbf{X}^{(i)} = \mathbf{B}^{(i)}, \tag{21}$$

with

$$\mathbf{A}^{(i)} = \begin{bmatrix} e^{-\boldsymbol{\eta}^{(i)} d_i} & \mathbf{1} & -\mathbf{1} & -e^{-\boldsymbol{\eta}^{(i+1)} d_{i+1}} \\ -\boldsymbol{\beta}^i e^{-\boldsymbol{\eta}^{(i)} d_i} & \boldsymbol{\beta}^i & \boldsymbol{\beta}^{i+1} & -\boldsymbol{\beta}^{i+1} e^{-\boldsymbol{\eta}^{(i+1)} d_{i+1}} \end{bmatrix} \tag{22}$$

$$\mathbf{X}^{(i)} = \begin{bmatrix} \mathbf{C}^{(i)} & \mathbf{D}^{(i)} & \mathbf{C}^{(i+1)} & \mathbf{D}^{(i+1)} \end{bmatrix}^T \tag{23}$$

and

$$\mathbf{B}^{(i)} = \left[\begin{array}{cc} \mathbf{0} & \delta_{i,0}\mathbf{C}^{(e)} \end{array} \right]^T. \tag{24}$$

The bold symbols in the system matrix (22) are understood as diagonal matrices, namely $\boldsymbol{\eta}^{(i)} = \mathrm{diag}\left[\eta_{mn}^{(i)}\right]$, $m = 0, \ldots, N_m$, $n = 0, \ldots, N_n$ and $\boldsymbol{\beta}^{(i)} = \kappa_i \boldsymbol{\eta}^{(i)}$, and the coefficient vectors such as $\mathbf{C}^{(e)}$ are column vectors, i.e., $\mathbf{C}^{(i)} = \left[C_{mn}^{(i)}\right]^{(i)}$, $m = 0, \ldots, N_m$, $n = 0, \ldots, N_n$, etc.

Assembling the relations (21) for the $N+1$ interfaces of the medium, we arrive at a linear system of equations, which relates the $2(N+1)N_mN_n$ sought development coefficients, *i.e.*, the system rank is $2(N+1)N_mN_n$. It should be noticed here that the inversion of (21) using algorithms for sparse matrices is equivalent to the explicit iterative calculation of (7), (12),(13) or the reflection/transmission coefficients approach adopted elsewhere, both from theoretical and computational point of view. The matrix form representation adopted in this work allows a more compact notation, which is the reason for choosing it.

2.4. Introduction of delamination defects

Let us consider now the multilayer medium of the previous paragraph but this time we assume an imperfect contact between the ith and the $(i+1)$th layer, which can be attributed to the existence of a thin void inclusion between the two layers. This kind of imperfect contacts between two adjacent layers is practically met in media affected by delamination defects. The effect of the defect on the heat propagation inside the medium can be taken into account by locally modifying the continuity relation between the two layers i and $i+1$.

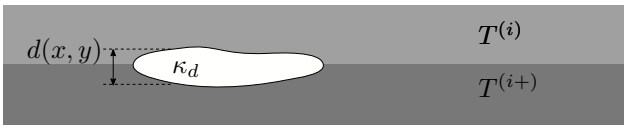

Figure 2: Void inclusion between two adjacent layers. The void is assumed homogeneous and much thiner than the embedding layers.

Consider the general case of a thin void inclusion depicted in Fig. 2, where $\mathscr{D}$ is void domain and $d(x, y)$ stands for its thickness, which in the general case is a function of the x, y position. By applying the Fourier's law across the void volume, one has

$$J_z = -\kappa_d \nabla T, \tag{25}$$

which for relatively small values of $d(x, z)$ reduces to the finite difference relation

$$J_z(x, y) \approx -\kappa_d \frac{T^{(i)}(x, y) - T^{(i+1)}(x, y)}{d(x, y)}. \tag{26}$$

By introducing the local thermal resistance as [28]

$$R(x, y) = \frac{d(x, y)}{\kappa_d}, \tag{27}$$

the previous relation can be written as follows:

$$T^{(i)} - T^{(i+1)} = -R(x, y)\, J_z. \tag{28}$$

Substitution of (28) into (19) and taking (16) into account yields

$$\begin{aligned} &\sum_{m'=0}^{N_m} \sum_{n'=0}^{N_n} \left(\delta_{nm,n'm'} - R_{m'n'} \kappa_i \eta_{m'n'}^{(i)} \right) C_{m'n'}^{(i)} e^{-\eta_{m'n'}^{(i)} d_i} \\ &+ \sum_{m'=0}^{N_m} \sum_{n'=0}^{N_n} \left(\delta_{nm,n'm'} + R_{m'n'} \kappa_i \eta_{m'n'}^{(i)} \right) D_{m'n'}^{(i)} e^{-\eta_{m'n'}^{(i)} d_i} \\ &- C_{mn}^{(i+1)} - D_{mn}^{(i+1)} e^{-\eta_{mn}^{(i+1)} d_{i+1}} = 0, \end{aligned} \tag{29}$$

where R_{mn} stands for the weighted thermal resistance function

$$R_{mn} = \int_{-L_x}^{L_x} \int_{-L_y}^{L_y} R(x, y)\, w(x, y)\, dxdy. \tag{30}$$

Adopting again the matrix notation presented above, the continuity relations for the ith layer become

$$\left(\mathbf{A}^{(i)} + \delta \mathbf{A}^{(i)} \right) \mathbf{X}^{(i)} = \mathbf{B}^{(i)} \tag{31}$$

with $\mathbf{A}^{(i)}$, $\mathbf{X}^{(i)}$ and $\mathbf{B}^{(i)}$ being given by (22), (23) and (24) respectively, and

$$\delta \mathbf{A}^{(i)} = \mathbf{R} \left[\begin{array}{cccc} -\boldsymbol{\beta}^i & \boldsymbol{\beta}^i & \mathbf{0} & \mathbf{0} \\ \mathbf{0} & \mathbf{0} & \mathbf{0} & \mathbf{0} \end{array} \right], \tag{32}$$

where this time $\mathbf{R}$ is a full matrix that couples all modes together. The introduction of the defect, in other words, comes at the cost of the partial loss of the system sparsity. An interesting limiting case, though, is the one where the support of the delamination defect exceeds the computational domain, i.e. $R(x, y) = c$, for $-L_x \leq x \leq L_x$ and $-L_y \leq y \leq L_y$, with c constant. In this case $\mathbf{R}$ becomes diagonal and the sparsity of the original system is restored. This is the quasi-1D case in the sense that the considered geometry is invariant along x and y directions, yet excited via an arbitrary flux profile. An intermediate case would be also having an infinite source along one of the x or y directions. In this latter case, the $\mathbf{R}$ matrix becomes block-diagonal, i.e., it has the form of a Kronecker product of a diagonal and a full submatrix.

2.5. Inverse Laplace transform

For the development of the semi-analytical solution we have worked so far entirely in the Laplace domain. We are interested though in the transient response of a number of observables such as the temperature evolution at specific points of the geometry and especially on the two surfaces of the medium, which is actually the only accessible experimental information of the method. In order to obtain the temporal evolution of the temperature field the solution in

the Laplace domain should be transformed back into the time domain.

There are several methods reported in the literature for performing this inversion. In this work we have chosen to carry out the inversion numerically using the Stehfest's algorithm [39, 40], which is an improved variant of Gaver's method [41]. This method is well adapted to the problem of impulse thermography studied here [28].

If $F(s)$ is the known Laplace transform of the function $f(t)$, evaluated at $s = a_j/t$ where $a_j = j\ln(2)$, then an approximate value of this function at time t can be calculated as

$$f(t) \cong \frac{\ln(2)}{t} \sum_{J=1}^{N} V_j F\left(j\frac{\ln(2)}{t}\right). \tag{33}$$

The coefficients V_j are given by the following expression for an even value of N:

$$V_j = (-1)^{j+N/2} \times \sum_{k=Int((j+1)/2)}^{Min(N/2,j)} \frac{k^{N/2(2k)!}}{(N/2-k)!k!(k-1)!(j-k)!(2k-j)!}. \tag{34}$$

In this equation 'Int' designates the integer part of a real number and 'Min' the minimum of two numbers.

Applying (34) at a number of preselected instances t, we then obtain the temporal profile of our observable at those points. The optimal choice of the points, itself, will depend on the thermal signal processing that we wish to apply. In the following, the TSR approach is used for the representation of the thermograms at the plate interfaces, and consequently the choice of the suitable sampling points will be based on this approach.

3. Defect shape reconstruction from the thermal images

In order to properly characterize subsurface defects in laminates, the signals recorded by an infrared camera should be processed by some algorithms. Data processing algorithms in TNDT are either one-dimensional or two-dimensional, with the first ones being applied to pixel-based temperature evolution in time and the second ones applied to single images. The time series of each recorded pixel is separately evaluated, usually to find any alterations of material' properties or the depth of those alterations. Single IR images are normally filtered or segmented to reduce random noise or to analyse geometrical features of the areas of interest.

Since its introduction [42], the thermographic signal reconstruction (TSR) method has emerged as one of the most widely used methods for enhancement, analysis and compression of raw thermographic sequences. The technique was originally developed for pulse thermography to improve contrast results and is one of the pixel-based methods.

One of the well-established edge-detection algorithms is the so-called Canny algorithm [24]. The methods processes an input image and detects the edges of any present objects (defects). Because of a better signal to noise ratio and detection accuracy, the Canny operator becomes the evaluation criterion of other methods. The algorithm consists of Gauss filtering, gradient calculation, non-maximum suppression, double thresholding, checking the edges and connecting the edges.

In this section, the theoretical background of the two mentioned methods is given and numerical results from their application for the detection of delamination-type defect in planar media shown.

3.1. Thermographic signal reconstruction

The technique is based on the pixel-based evaluation of the time series which represent the surface temperature variation over time. The technique consists of two basic steps. The first step is the fitting of the recorded time series in the log-log space by a logarithmic polynomial of degree n. This step provides a significant compression of the raw data. In a later step, the reconstruction of the temperature signals in the logarithmic domain using the polynomial has to be performed, providing noise-reduced copy of each pixel time series. Fitting to the thermograms highly depends on the time window chosen and the polynomial degree. Thus, the choice of the time window has to be made with the objective to consider only the part of the thermograms influenced by the physical phenomena to characterize, and the polynomial degree has to be defined considering that this will be a trade-off between accuracy of signal reproduction and denoising.

Especially, in a defect-free sample, the thermal diffusion in the lateral direction could be neglected compared to the normal direction, so one can consider the one-dimensional heat equation for the thermography. In principle, the method exploits the well-known observation that in a semi-infinite flawless sample, or in a very thick slab, the surface temperature response to instantaneous uniform heating, ideal impulsive heat flux, is described by the one-dimensional heat diffusion equation

$$\frac{\partial T}{\partial t} = \alpha \frac{\partial^2 T}{\partial z^2}, \tag{35}$$

where $\alpha = \frac{\kappa}{\rho c}$ is the thermal diffusivity of the material with the solution

$$T(z,t) = \frac{Q}{\epsilon\sqrt{\pi t}} e^{\frac{z^2}{4\alpha t}} \tag{36}$$

at distance z from its surface, where $\epsilon = \sqrt{\kappa\rho c}$ is the heat effusivity and Q is the quantity of energy absorbed by the surface. Since thermal imaging is only applicable to surface temperature, from Eq. (36) one has the temperature increase ΔT (thermogram) as a function of time t at the surface:

$$\Delta T(t) = \frac{Q}{\epsilon\sqrt{\pi t}}. \tag{37}$$

The one-dimensional approximation of Eq. (37) assumes that the lateral diffusion components more or less cancel in a defect-free sample. However, in the presence of an adiabatic subsurface boundary such as a void, a wall, a buried defect, or in the case of a multi-layer sample the incident heat flow from the sample surface is impeded, and this solution no longer applies locally. The effect of a wall is shown in the left plot in Fig. 3 where the surface temperature for a semi-infinite sample is compared with the case of the presence of an adiabatic wall at three different depths. The effect of a buried defect in the thermograms is shown in the right plot in Fig. 3 where the separation of the temperature response at the surface of a solid between a sound area and a defected area should be simple when these defects are large or very close to the surface. However, when one attempts to detect thin buried defects, the effects of infrared camera noise as well as the complexity found in many samples limit the ability to discriminate between sound and flawed areas.

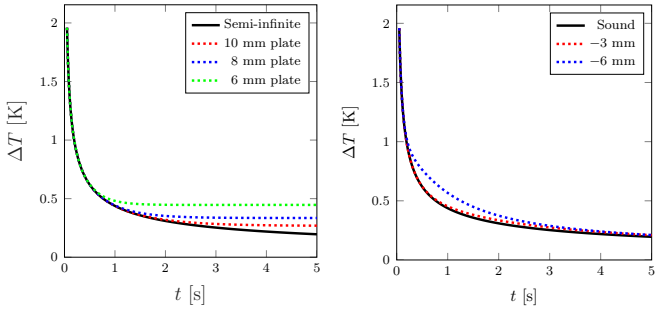

Figure 3: Surface temperature decay curves for a single point of a steel plate. *Left:* Comparison of temperature time plot of a semi-infinite sample with three adiabatic samples of different thickness. *Right:* Comparison of temperature time plot of a sound sample with two defected samples at different depth.

Considering the time evolution of the surface temperature in the logarithmic domain, where Eq. (37) can be written in the logarithmic scale, additional insight into the surface temperature response during the cooling period of the sample is gained:

$$\ln\left(\Delta T\right) = \ln\left(\frac{Q}{\epsilon\sqrt{\pi}}\right) - \frac{1}{2}\ln\left(t\right). \tag{38}$$

In Eq (38) the time dependence has been separated from the input energy and material properties. Only the offset of the response will change as the sample material and the input energy vary.

For a semi-infinite piece, Eq. (38) describes a straight line with slope equal to $-1/2$, as pictured in Fig. 4. In the case of an adiabatic plate, the response deviates from the straight line at a particular time, depicted in the left plot in Fig. 4. This particular time is correlated with the thickness of the plate. In the presence of a subsurface defect in a plate, or in a semi-infinite solid, the time evolution plot of the temperature corresponding to those pixels depart from that behaviour in a particular time but in a different way comparing to the case of the adiabatic flaw-free plate, as shown in the right hand plot in Fig. 4.

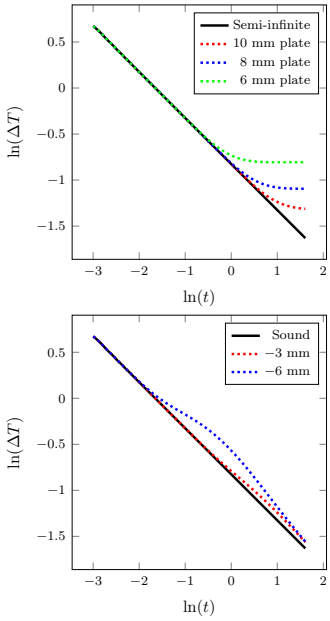

Figure 4: Surface temperature decay curves for a single point of a steel plate in the logarithmic scale. *Left:* Comparison of temperature time plot of a semi-infinite sample with three adiabatic samples of different thickness in the logarithmic space. *Right:* Comparison of temperature time plot of a sound sample with two defected samples at different depth in the logarithmic space.

In Fig. 4 the thermograms have been normalised based on Eq. (38) where the term which describes the source and the material effect have been removed.

For a given pixel, the response given by Eq. (38) can be approximated, in general, by a function or set of orthogonal functions. The TSR method uses a polynomial series to fit the experimental data in log-log space:

$$\ln\left(\Delta T\right) = \sum_{n=0}^{N} a_n \left[\ln(t)\right]^n. \tag{39}$$

The fitting of the log-log thermogram, for each recorded pixel (i, j), by the logarithmic polynomial replaces the full sequence of the temperature response images $T(i, j, t)$ by the series of $(n + 1)$ images of the polynomial coefficients $a_0(i, j), \cdots, a_n(i, j)$. Once the time evolution of each pixel has been approximated by Eq. (39), the original data can be reconstructed as

$$\Delta T = \exp\left(\sum_{n=0}^{N} a_n \left[\ln(t)\right]^n\right). \tag{40}$$

Thus, it is only necessary to store the polynomial coefficients a_n and reconstruct the images stack at required time samples. This approach provides a significant degree of data compression.

A low–degree polynomial expansion is applied usually to serve as a low–pass filter. Thus, this approximation pre-

serves the essential thermal response, while rejecting non–thermal noise contributions. The use of higher-order polynomials reproduces the original data and replicates also part of the noise that appears in the later, low–amplitude data. In Fig. 5 reconstructed noisy signals by using polynomial degrees $n = 7$ and 17, with and without the presence of a defect, are compared, and the trade-off between accuracy of signal reproduction and signal denoising is clearly exhibited.

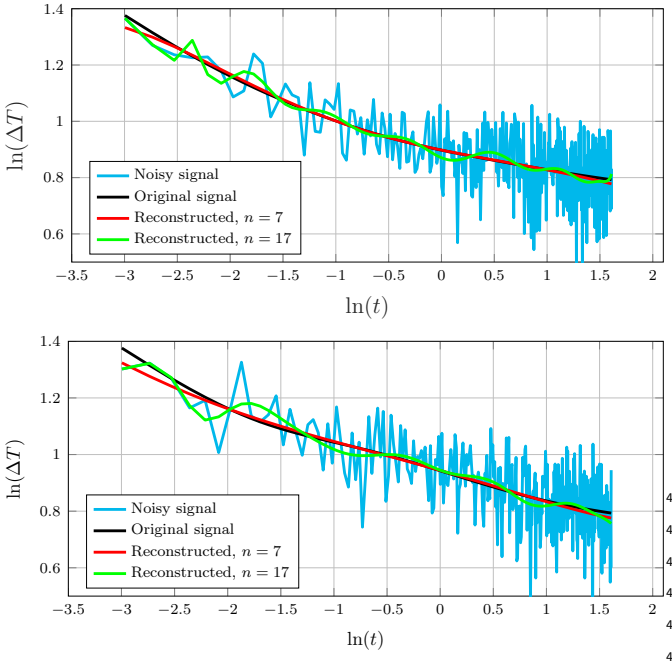

Figure 5: Regression by a logarithmic polynomial of degree n equal to 7 and to 17, for a sound area, in the top plot, and a flawed area, in the bottom plot.

The use of TSR effectively removes the temporal noise from the recorded raw signals. However, the reduction of temporal noise does not necessarily increase the flaw detectability. This can be partially addressed by the computation of the first and second time derivatives, using Eq. (39), without additional noise contributions, which leads to equations

$$\frac{\mathrm{d}\ln(\Delta T)}{\mathrm{d}[\ln(t)]} = \sum_{n=1}^{N} n a_n [\ln(t)]^{n-1}, \quad (41)$$

$$\frac{\mathrm{d}^2\ln(\Delta T)}{\mathrm{d}[\ln(t)]^2} = \sum_{n=2}^{N} n(n-1) a_n [\ln(t)]^{n-2}, \quad (42)$$

for the first and the second derivative, respectively. The temperature in the logarithmic scale is compared with the first and the second time derivative for a sound area and a flawed area in Fig. 6.

The denoising provided by TSR is not limited to the time signals but has been partially transmitted to the spatial signals also, this is an indirect effect of the method. The derivatives, by definition, are much more sensitive to

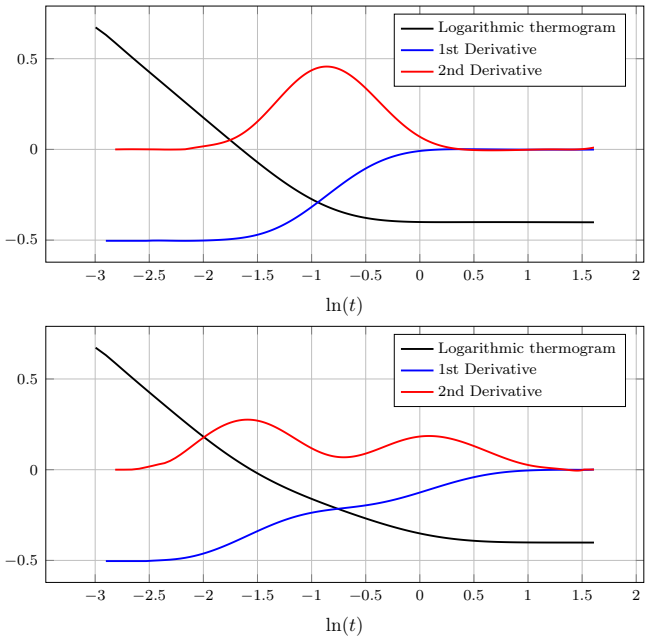

Figure 6: Plots of the logarithmic thermogram, 1st and 2nd logarithmic time derivatives for a thick steel plate. *Top:* Homogeneous sound plate. *Bottom:* Homogeneous plate with an embedded flaw.

small changes in amplitude than the raw signal. However, after the application of the TSR that acts as a low-pass filter, the derivatives are less sensitive to random signal fluctuations. In Fig. 7 the raw signals versus the horizontal position plot of the steel defect sample and the TSR first derivative are compared.

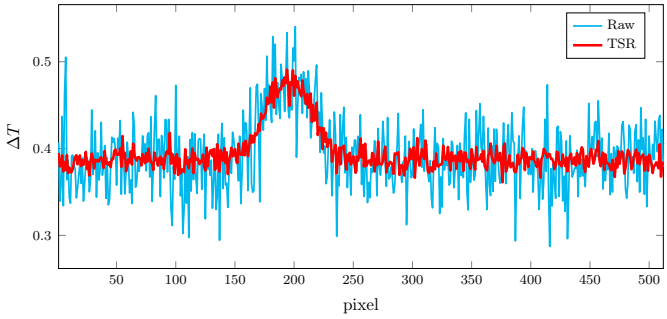

Figure 7: Comparison of raw and TSR results for a horizontal line through the centre row of delamination.

The derivative signals have been partially denoised by TSR also. The high sensitivity of the derivatives to small changes makes them ideal for the detection of features that can be undetectable in the original data. Comparing now images obtained from TSR, first and second derivatives, in Fig. 8, it is obvious that the images are sharper and the detectability of small flaws has been significantly improved.

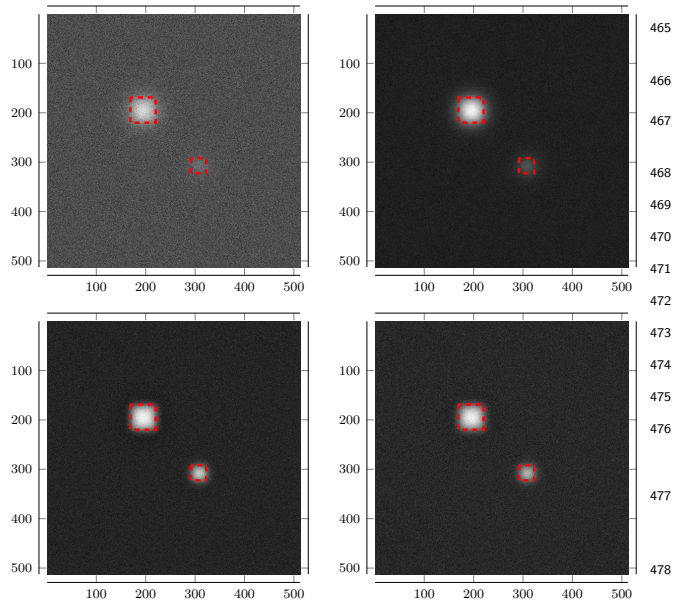

Figure 8: Comparison of raw image in the left top corner, TSR image in the right top corner, 1st derivative image in the left bottom corner and 2nd derivative image in the right bottom corner.

3.2. Shape reconstruction using the Canny edge detection algorithm

In its classical form, the Canny algorithm, in its first step, processes the image smoothly through Gaussian convolution and obtains the gradient image through differential operation on the image which is processed via Gaussian convolution. Consider the two-dimensional Gaussian function

$$G(x,y) = \frac{1}{2\pi\sigma^2}\exp\left(-\frac{x^2+y^2}{2\sigma^2}\right), \tag{43}$$

with mean $\mu = 0$ and standard deviation σ. The parameter σ is the width of the Gaussian filter and directly determines the effect of filtering where larger σ provides smoother images. The filtered image is derived from the convolution

$$\widehat{\mathscr{I}}(x,y) = G(x,y) * \mathscr{I}(x,y), \tag{44}$$

where $\mathscr{I}(x,y)$ is the original image matrix. Making use of Gaussian function's separability, ∇G can be decomposed into two one-dimension filters:

$$\frac{\partial G}{\partial x} = kx\exp\left(-\frac{x^2}{2\sigma^2}\right)\exp\left(-\frac{y^2}{2\sigma^2}\right), \tag{45a}$$

$$\frac{\partial G}{\partial y} = ky\exp\left(-\frac{y^2}{2\sigma^2}\right)\exp\left(-\frac{x^2}{2\sigma^2}\right). \tag{45b}$$

By convolving these equations with the image we obtain:

$$L_x = \frac{\partial G}{\partial x} * \mathscr{I}(x,y), \tag{46a}$$

$$L_y = \frac{\partial G}{\partial y} * \mathscr{I}(x,y), \tag{46b}$$

where in a matrix representation this can be written as:

$$L_x = K_x * \mathscr{I}(i,j), \tag{47a}$$

$$L_y = K_y * \mathscr{I}(i,j), \tag{47b}$$

where i and j are the coordinates of a pixel in the image.

This is a way to compute the gradient, but not the only one. Different kernels can be used to calculate the image gradient. This could separate the denoising part of the algorithm from the computation of the gradient. For the traditional Canny algorithm, two 2×2 convolution operators K_x and K_y are deployed to calculate the image gradient in the x and y directions, respectively. These operators are written as:

$$K_x = \begin{bmatrix} 1 & -1 \\ 1 & -1 \end{bmatrix}, \tag{48a}$$

$$K_y = \begin{bmatrix} 1 & 1 \\ -1 & -1 \end{bmatrix}. \tag{48b}$$

In general, 2×2 or 3×3 kernels based on finite differences are used for the computation of the gradient. In the literature one can find many other derivative kernels which provide also some smoothing in the data, with the most used ones being the Sobel operator:

$$K_x = \begin{bmatrix} 1 & 0 & -1 \\ 2 & 1 & -2 \\ 1 & 0 & -1 \end{bmatrix}, \tag{49a}$$

$$K_y = \begin{bmatrix} 1 & 2 & 1 \\ 0 & 1 & 0 \\ -1 & -2 & -1 \end{bmatrix}. \tag{49b}$$

After convolving the image with the kernels, the gradient-component intensity of the image is derived from

$$M(i,j) = \sqrt{L_x^2(i,j) + L_y^2(i,j)}, \tag{50}$$

and its normal vector direction at the pixel (i,j) is defined as

$$\theta(i,j) = \arctan\left[\frac{L_x(i,j)}{L_y(i,j)}\right]. \tag{51}$$

To follow, after smoothing the image using Gaussian smoothing and convolving it with derivative kernels, one ends up with the gradient magnitude image $M(i,j)$ which reflects the edge intensity at the pixel (i,j), and $\theta(i,j)$, which reflects the normal vector at the pixel (i,j) in the image. Edges of objects can be extracted from the gradient component intensity image, but they will be quite blurry. In this step, the algorithm aims at thinning those edges by setting the pixels around local maxima in the gradient image M to 0.

Firstly, the direction angle is rounded to 0°, 45°, 90°, 135° for the relative position in adjacent pixels of the image. Aiming at every pixel whose value is non-zero, the gradient-component intensity of a candidate pixel $M(i,j)$ is compared with two adjacent pixels along the rounded direction angle. The candidate pixel is preserved only if

its gradient component intensity is the largest. Otherwise, it is set to zero. Let the processed image be $\widehat{M}(i,j)$.

The non-maximum suppression gives the non-zero pixels providing more accurate approximation regarding the edges of the objects in the processed image $M(i,j)$. These pixels are taken as the edge pixels. Due to noise in the original image, $\widehat{M}(i,j)$ contains pixels depicting false edges, the spurious edge response. To mitigate these spurious edges, hysteresis tracking is performed using dual thresholding by setting a high τ_h and a low τ_l threshold parameter. Edge pixels which have gradient larger than τ_h are added automatically to the final binary image and are considered as strong edge pixels. In opposition, edge pixels with a gradient lower than τ_l are considered as phantom edges and are discarded. The remaining pixels with a gradient value between τ_l and τ_h are considered as weak edges and are added to the final binary image only if they are connected with a strong edge pixel. When none of the 8-connected neighbourhood pixels is a strong pixel, the candidate pixel is suppressed.

The choice of thresholds is very crucial for the success of the method. The algorithm can wipe off most of the spurious edges while increasing the value of τ_h, but meanwhile, some edges may be missed. On the other hand, by decreasing the value of τ_l more information about the edges will be preserved but the edge's characteristic will become less and less at the point where the true edges will be missed. Auto-select thresholding value is a difficult task. At present, there are many kinds of methods in selecting threshold values. The more widely used is the Otsu method [43] but also other methods based on histogram, maximum entropy, or statics are used [44, 45, 46].

The Otsu method has the best threshold value in the statistical sense and is the most stable method in the image threshold segmentation. The method has been used here to choose the value of τ_h automatically. The method assumes that the pixels of the image to be thresholded can be separated into two classes, *e.g.* foreground and background, then calculates the optimum threshold separating those two classes so that their combined spread is minimal.

Suppose that $G = [0, L-1]$ is the range of greyscale in image F and P_i is the probability of every greyscale and the threshold value τ has splitted the image in two classes which are $C_0 = [0, \tau]$ and $C_1 = [\tau + 1, L-1]$. The two classes probabilities are

$$\alpha_0 = \sum_{i=0}^{\tau} P_i$$

and

$$\alpha_1 = 1 - \alpha_0,$$

respectively. The average grey values of the two classes are

$$\mu_0 = \sum_{i=0}^{\tau} \frac{iP_i}{\alpha_0} = \frac{\mu_\tau}{\alpha_0}$$

and

$$\mu_1 = \sum_{i=\tau+1}^{L-1} \frac{iP_i}{\alpha_1} = \frac{\mu - \mu_\tau}{1 - \alpha_0},$$

respectively, therein

$$\mu = \sum_{i=0}^{L-1} iP_i, \qquad \mu_\tau = \sum_{i=0}^{\tau} iP_i.$$

The criterion function has been defined as variance between the two classes, expressed as

$$\eta^2(\tau) = \alpha_0 (\mu_0 - \mu)^2 + \alpha_1 (\mu_1 - \mu)^2 \quad (52)$$

$$= \alpha_0 \alpha_1 (\mu_0 - \mu_1)^2 . \quad (53)$$

The optimal threshold value $\tau^\star$ is given by

$$\eta^2(\tau^\star) = \max_{0 \le \tau \le L} \eta^2(\tau). \quad (54)$$

Threshold $\tau^\star$ will be used as the high threshold parameter τ_h. The value of the low threshold τ_l, usually, is set to be $\tau_l = \frac{\tau_h}{2}$.

The last step of the algorithm is the connection of already detected edges on the binary image under some restrictions. These restrictions are criteria set upon the gradient value $\widehat{M}(i,j)$ and the gradient angle $\theta(i,j)$ of the non-edge pixels between two edges. If the gradient is larger than a given value and the gradient angle is close to zero, the pixels between the two edges are added to the binary image.

The output of the Canny algorithm is a binary image which contains the edges of any object present in the initial image.

4. Results

4.1. Description of the configuration

In this section, the proposed multi-step flaw characterization technique will be demonstrated by employing the forward model developed in Sec. 2, and the image processing techniques described in Sec. 3. Temperature signals, produced by the three-dimensional TREE model, have been corrupted with Gaussian noise of different levels to simulate temperature signals collected by an infrared camera and from now on are called raw signals. Other types of noise beyond Gaussian could be used in this part but this is out of our scope. The detection and characterization procedure has been divided into two parts.The first step concerns the detection and shape reconstruction of candidate flaws and the second step, their characterization through an iterative parameter estimation technique regularised by the information gained from the first step.

Concerning this section, the three-dimensional model developed in Sec. 2 has been used to compute the temperature field, for the general configuration depicted in Fig. 9.

These signals are supposed to be collected at the front, or upper surface of the work piece. A grade 4340 steel plate

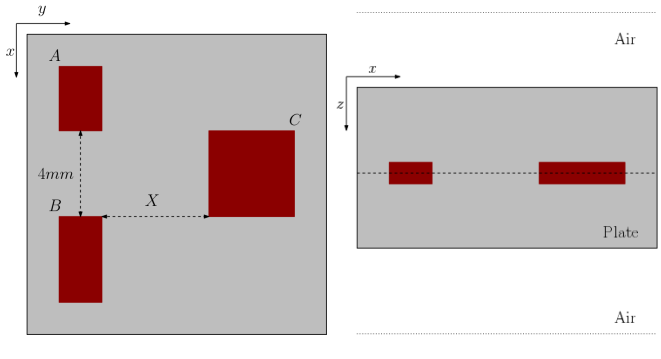

Figure 9: Sketch of the configuration in the (x, y) and (x, z)–plane, left and right respectively.

with thermal conductivity $k = 44.5$ W/mK, heat capacity $C_p = 475$ J/kgK, density $\rho = 7850$ kg/m^3 and thickness $d = 3$ mm is used. The plate is considered to be infinite in the x– and y–direction where the area of interest is a 40×40 mm^2 rectangle. Three well-defined air-filled defects, named A, B and C, which simulate delaminations of different thickness, $d_A = 3 \times 10^{-3}$ mm, $d_B = 2 \times 10^{-3}$ mm, $d_C = 1 \times 10^{-3}$ mm and of different sizes 3×2 mm^2, 4×2 mm^2, 4×4 mm^2, respectively, have been embedded into the plate with their larger faces set to be parallel to the plate surface. As an excitation term, a flash lamp, set above the plate and parallel to its surface, depositing a heating power density of Q $= 10^4$ W/m^2 at the surface of the plate, has been modelled as a Dirac's delta function in time, whereas its spatial distribution is considered to be uniform and covers all the domain of interest, as already done before.

4.2. TSR and noise reduction

The described configuration is used in this part with the addition that the flaws are located in the middle of the plate along the z–axis.

The shape reconstruction part of the technique starts by applying the TSR method to the noisy signals. This provides the polynomial approximation of the signals, say, the matrix $\mathscr{P}$ of dimensions $N_x \times N_y \times (p+1)$, where N_x, N_y are the pixels numbers along the x– and y–directions, and p is the polynomial degree. Polynomial coefficients of the first and second time derivatives are stored in the matrices $\mathscr{P}_1$ and $\mathscr{P}_2$, respectively. The time-dependent temperature field in the logarithmic scale, as well as the first and second time derivatives, can be reconstructed using the polynomial matrices $\mathscr{P}, \mathscr{P}_1, \mathscr{P}_2$ and stored in the matrices $\mathscr{I}, \mathscr{I}_1, \mathscr{I}_2$. The reconstruction of the time signals derives time frames which are smoother and suitable for defect detection. The reconstructed second time derivative matrix, $\mathscr{I}_2$, will be used for the detection of the time which corresponds to the best frame.

The choice of the polynomial degree is a very crucial task for the TSR technique, here we choose to work with 7^{th} degree polynomials that were shown to approximate the original signal with high accuracy and filtering most of the noise as observed from the log – log plots in Fig. 5. In Fig. 10 the reconstructed signals versus time are compared with the raw noisy signals as well as with the synthetic signals as a reference. The signals correspond to two different pixels with the first one being at the centre of the plate where it is considered to be a sound area and the second one at the centre of the largest defect, named C, left hand and right hand plot in Fig. 10, respectively. It is clear from Fig. 10 that most of the noise has been significantly filtered through the TSR method and the original signals have been reconstructed with great accuracy.

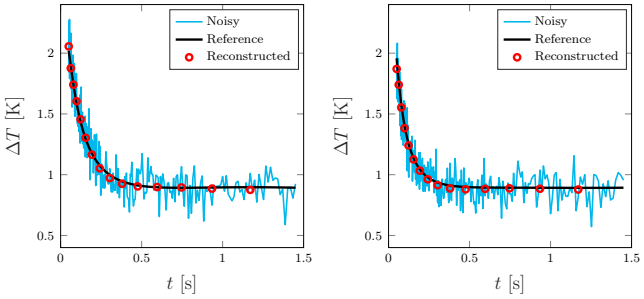

Figure 10: Reconstruction of temperature noisy signals with the TSR technique for a sound area and a flawed area. Comparison of the reconstructed signals with the reference signals and the noisy signals. *Left:* Time signals corresponding to a sound area of the plate. *Right:* Time signals corresponding to a flawed area of the plate.

An additional important detrimental factor for the raw signal is the finite camera readout precision, which is superposed to the additive signal noise. In order to test the algorithm robustness under more realistic conditions of finite camera readout, a minimum temperature resolution has been assumed, resulting in a rounded raw temperature signal with a precision of 0.05°C. The raw signal deformation when a finite precision is considered is shown in Fig. 7. In the same figure is also given the comparison of the resulting signal with infinite and finite temperature resolution after the application of the TSR. As can be seen from the comparison, the finite round-off error of the camera has a visible impact on the raw signal itself, yet the effect is relieved to a satisfactory degree when applying the TSR algorithm. Note that the two TSR signals (with zero and finite round-off error) have been obtained using the same polynomial degree.

4.3. Shape reconstruction

The choice of the most suitable frame for shape reconstruction is crucial at this point. The best frame for the shape reconstruction algorithm should correspond to a time instant which maximises the contrast of the image. The contrast for defects of different thicknesses, located at different depths, reach their maximum contrast at different times [13]. To compute the contrast, one needs information about where the flaws are located and a reference sound area. Since no reference data will be used, so the computation of the contrast could be considered as

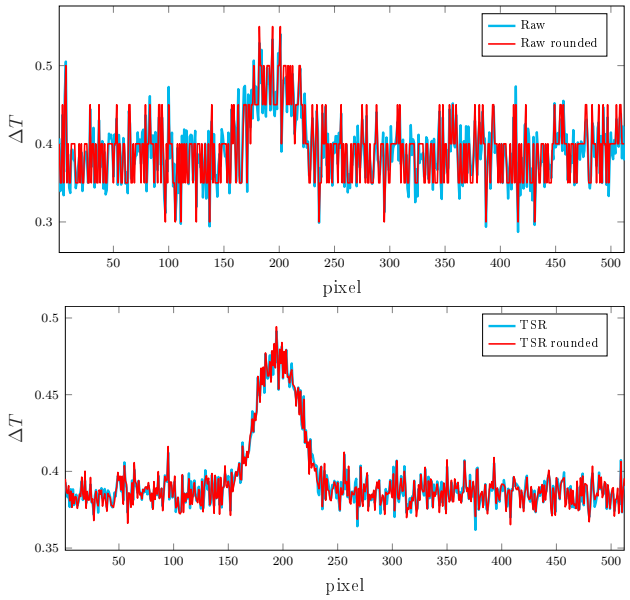

Figure 11: Comparison of the thermal signal obtained using zero and finite round-off error for a horizontal line through the centre row of delamination. *Up:* Raw signal. *Down:* Signal after application of the TSR algorithm. The TSR seems to remove the finite precision effect yielding an SNR comparable with the one obtained for zero round-off.

an option, the second time derivative matrix $\mathscr{I}_2$ will be used. A criterion upon the second time derivative for each pixel will be set instead. Each variation that occurs in the time-dependent signals, which is a result of the alteration of material thermal properties at a specific depth, is indicated by a change of the first time derivative of the signals. This change on the first time derivative of the signal causes the second time derivative to change significantly. The times at which the second time derivative reaches its local maxima are correlated with the times where the absolute contrast of the second derivative reaches its local maxima. In order to have an early flaw identification, and avoid the image blurring at later times, we take into account the times where the second time derivative changes sign. For each frame, the frequency of the sign changes of the second time derivative will be computed and the frame with the maximum frequency chosen as shown in Fig. 12, where the maximum frequency has been marked with a red asterisk. If we have more than one candidate frame, the frame that corresponds to the earlier time will be chosen. This results in a sharper image but in a multilayer configuration could result in loss of information about deeply buried defects, i.e. very close to the bottom surface. In such a case multiple images could be used.

The image corresponding to that frame number is shown in Fig. 13, left, and been named $\mathscr{I}^*$. The effect of the technique on partially denoising the signals in space can be seen by the comparison of the derived image with the raw image corresponding to the same frame number, Fig. 13, right. An RGB image constructed from the triplet $\mathscr{I}^*$, $\mathscr{I}_1^*$, $\mathscr{I}_2^*$ is shown in Fig. 14. The later is useful in understanding the relative depth of the flaws and their relative thickness since flaws with significantly different thickness or located at different depth will appear with different colours.

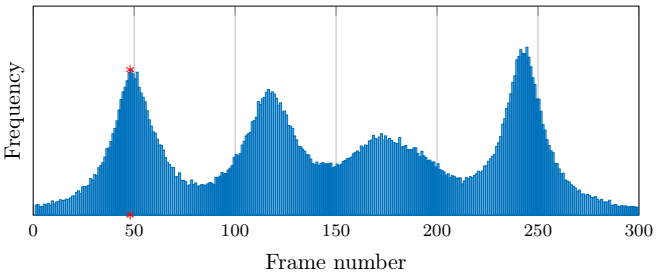

Figure 12: Frequency of the sign changes of the second time derivative for all pixels in each frame of the reconstructed signals.

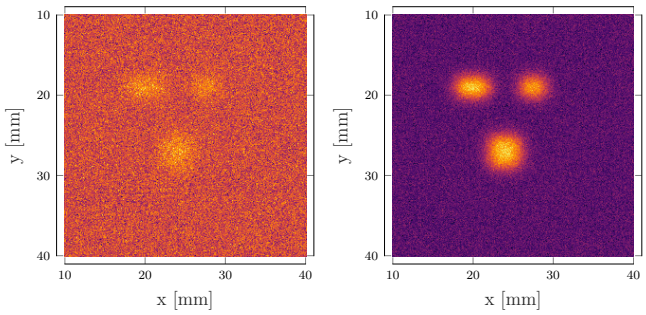

Figure 13: Comparison of a raw image with the reconstructed image corresponding to the same optimal frame number. *Left:* Raw image, $\mathscr{I}$. *Right:* Reconstructed image, $\mathscr{I}^*$.

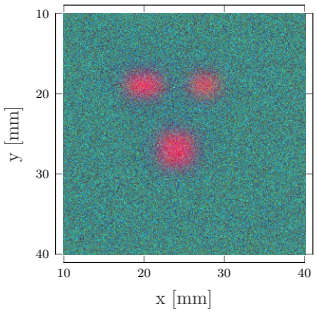

Figure 14: RGB($\mathscr{I}^*, \mathscr{I}_1^*, \mathscr{I}_2^*$) image corresponding to the optimal frame number.

A similar RGB image can be constructed from the monomials but that representation is quite noisy when a high degree polynomial is used. The degree of the polynomials used here, $p = 7$, is considered to be high compared with the short time period of the recorded signals and the noise level. For a longer time period or lower noise level, an RGB image reconstructed using the monomials could be as useful as the image in Fig. 14. We illustrate this in Fig. 15, where signals with higher SNR (40 dB) are used to reconstruct RGB images using 5^{th} and 7^{th} degree polynomials. In Fig. 15, left, the monomials $-5/5, 4/5, 3/5$ are used to

form the image and in Fig. 15, right, the used monomials are the $-7/7, 6/7, 5/7$. It is clear from the figures that a lower degree polynomial will offer more qualitative information about the flaws that a higher degree polynomial which inherits a larger part of noise.

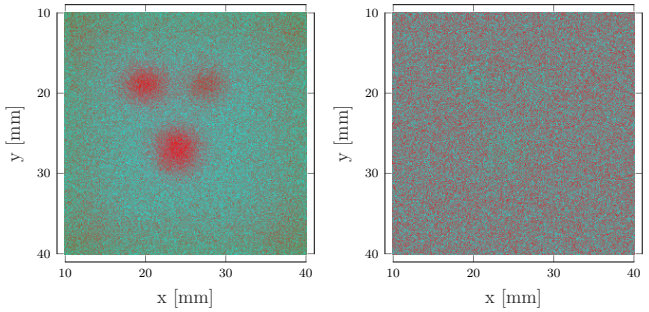

Figure 15: Reconstructed RGB image from the projection of three monomials after applying TSR on signals with SNR = 40 dB using polynomials of 5^{th} degree, *left*, and 7^{th} degree, *right*.

At this point, the image $\mathscr{I}^*$ will be provided to the Canny algorithm for the detection and the reconstruction of defects' shape. The first step of the algorithm consists of a Gaussian smoothing of which the image will be a subject. Thus the parameter σ that defines the amount of smoothing will be provided to the Canny algorithm since the smoothing algorithm has been integrated into the Canny algorithm. In our case, we perform a slight smoothing by using $\sigma = 5$. A comparison in greyscale of the input image and the smoothed one is shown in Fig. 16, where the two images have been rescaled.

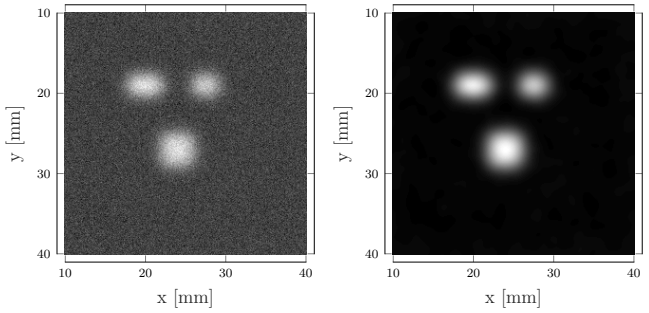

Figure 16: The impact of the Gaussian smoothing of the input image to the Canny algorithm shown in grey scale. *Left:* The noisy input image $\mathscr{I}^*$. *Right:* The smoothed image $\widehat{\mathscr{I}^*}$.

A gradient magnitude image M, Fig. 17, left, of the smoothed image $\widehat{\mathscr{I}^*}$, Fig. 16, right, will be derived after its convolution with the derivative kernel, and in this case, the Sobel kernel has been used. By applying non-maximum suppression to the gradient image, all values along the line of the gradient that are not peak values of the ridge have been suppressed. This leads to the image $\widehat{M}$, Fig. 17, right, which contains one-pixel- wide edges.

Due to noise in the original image, $\widehat{M}$ contains pixels depicting false edges and to mitigate these spurious edges, hysteresis tracking is performed using dual thresholding.

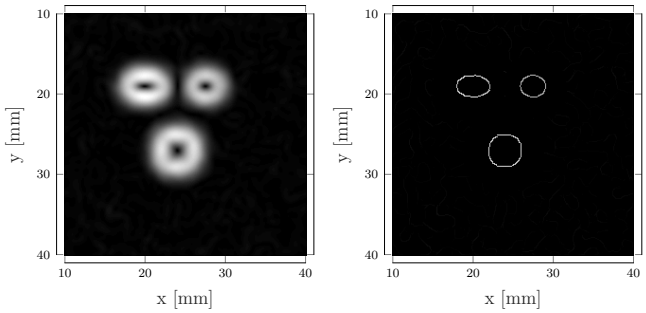

Figure 17: The impact of the non-maximum suppression on the gradient intensity image. *Left:* The gradient intensity image before applying non-maximum suppression, $M(i, j)$. *Right:* The gradient intensity image after applying non-maximum suppression, $\widehat{M}(i, j)$.

The choice of the threshold parameters is crucial for the success of the method, so we use the Otsu [43] method to compute these parameters. The method provides the high threshold parameter τ_h, and the low threshold parameter τ_l will be set by us, $\tau_l = \tau_h/2$. Pixels that correspond to values higher than the high threshold are considered strong edges and preserved, pixels that fall under the low threshold are omitted. Pixels that fall between the two threshold parameters are considered as weak edges and kept only if connected with a strong edge. The last step of the algorithm is the connection of already detected edges in the binary image under some restrictions upon the gradient and the gradient angle.

The stages of the edge detection for the three individual defects are shown in Fig. 18, where different colours refer to different stages of the detection. The strong edges detected after the non-maximum suppression are coloured in blue. In green and red, are the parts of the edge omitted or added after the hysteresis tracking, respectively. The green part of the edges is the last added part during the connectivity analysis.

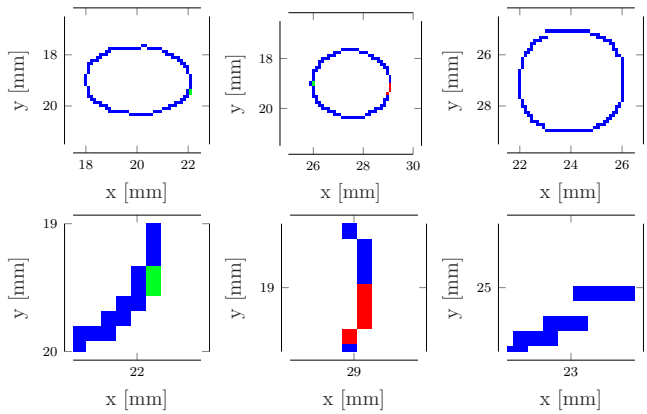

Figure 18: The stages of the edge detection algorithm illustrated with different colours.

The final binary image which gives the edges of the flaws is depicted in Fig. 19 where the true shape of the defects is depicted with green colour lines.

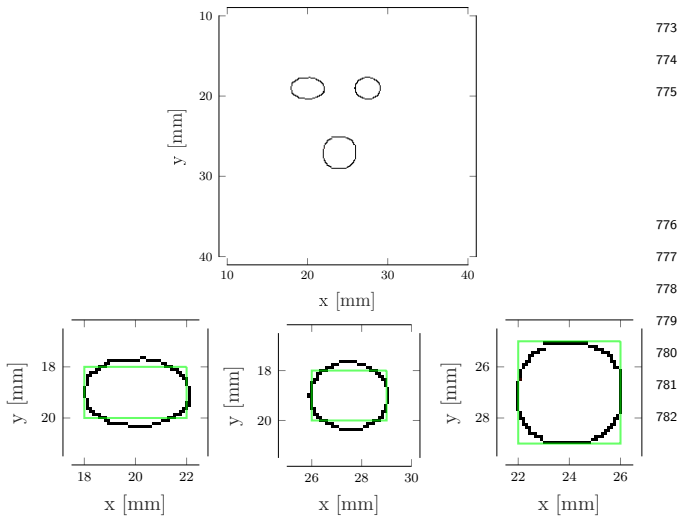

Figure 19: The final binary image.

The presented multi-step procedure was fully automated exempt the fact that the smoothing parameter σ is needed to be given. By giving a different value to this parameter the results will change but in our case not dramatically as can be seen in Fig. 20, where the smoothed input image is given, for $\sigma = 3$, and the final reconstructed binary image.

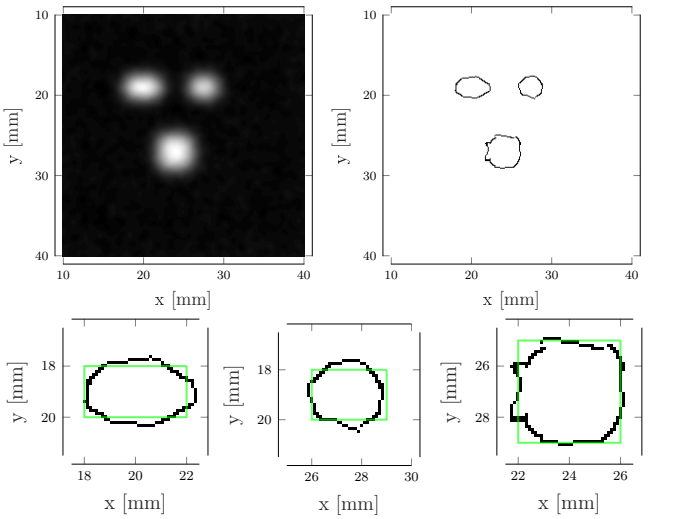

Figure 20: Gaussian smoothing of the input image to the Canny algorithm shown in grey scale. *Left:* The noisy input image $\mathscr{I}^*$. *Right:* The smoothed image $\widehat{\mathscr{I}^*}$.

4.4. Non uniform heating

The previous results have been produced under the assumption of an ideal homogeneous heating. In reality, a number of factors such as the finite camera support, its position and orientation, local variations of material properties, etc. can introduce gradients into the heat front profile. In order to study the impact of this effect on the reconstruction results, the profile of the impinging flux has been modified by introducing a gradient along the x direction as follows

$$J_e(x,y) = -\left[1 - \sin(\phi_x)\frac{x - x_1}{x_2}\right] k^{(1)} \frac{\partial \widehat{T}^{(e)}}{\partial z} \qquad (55)$$

where x_1 and x_2 are the limits of the flash support in the x–direction. This excitation term leads to an uneven heating of the piece in the x-direction, with the left side being heated more than the right one.

The TSR results for the best contrast image for $\phi_x = 5$ and $\phi_x = 30$ with an SNR equal to 10 dB are shown in Fig. 21. The corresponding results of the Canny algorithm for the edge detection are given in Fig. 22.

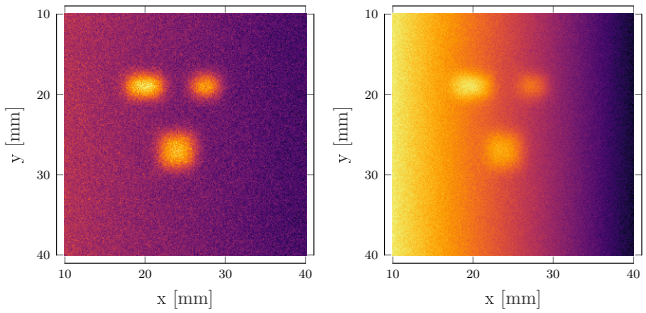

Figure 21: Best TSR reconstructed frame with different heat-front gradient. *Left:* $\phi_x = 5$. *Right:* $\phi_x = 30$

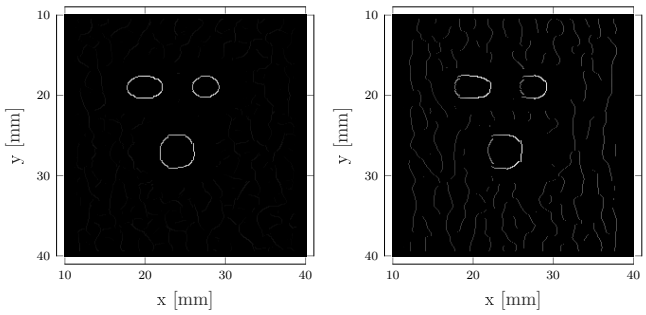

Figure 22: Results for the edge detection obtained using the frames of Fig. 21 after application of non-maximum suppression. *Left:* $\phi_x = 5$. *Right:* $\phi_x = 30$

Being relatively smooth, the gradient of the thermal field does not seem having a severe impact to the reconstruction images (cf. Fig. 21). As far as the edge detection is concerned, the algorithm seems to be relatively insensitive, with a weak variation of the edge stroke being visible for the stronger gradient ($\phi_x = 30$).

It must be underlined however that the above conclusions apply as far as the field gradient is relatively low-frequency, in other words smooth with respect to the sought defect. This assumption is met for sources with extended illumination support, such as flash lamps considered in this work. The algorithm is expected to be less

robust when point-wise heating, using Laser sources for example, is applied.

4.5. Depth effect

The reconstruction results are expected to be also dependent from the depth of the defects, since the primary field of the heat source becomes more diffuse. This effect is important, when the inspection is carried out from the opposite side of the excitation (transmission thermography). In order to test the algorithm performance with increasing defect depth, the simulations have been carried out for three different depths, namely $z = 0.75$mm, $z = 1.5$mm and $z = 2.25$mm, and the reconstruction algorithm has been applied using the corresponding noise-corrupted images. The raw and TSR reconstructed results for the optimal-contrast frame are shown in Fig. 23. The SNR has been set equal to 10 dB.

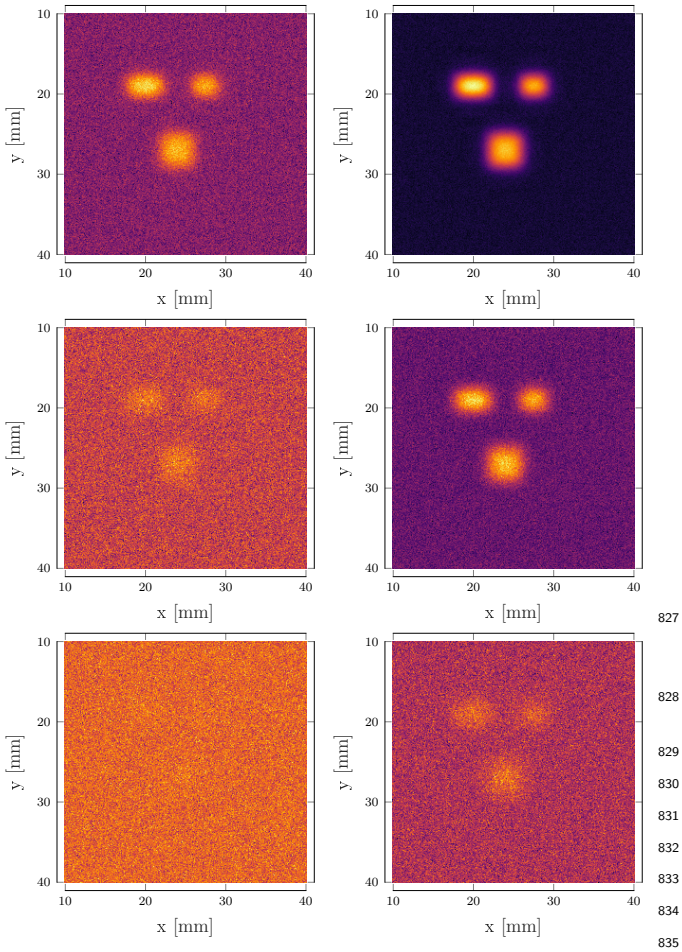

Figure 23: Comparison of a raw image with the reconstructed image corresponding to the same optimal frame number for three different defect depths $z = 0.75$mm, $z = 1.5$mm and $z = 2.25$mm. *Left Column:* Raw images. *Right Column:* Reconstructed images.

From the illustrated results the beneficial effect of the TSR-induced denoising becomes evident and the resulting enhancement of the edge detection algorithm is obvious.

4.6. Complex defect shapes

For a better judgement of the reconstruction capabilities in the case of defects with more complex shapes, the proposed algorithm has been applied in the case of a circular and an irregular shaped defect, whose geometries are given in Fig. 24. In the same figure are illustrated the edges forms obtained after the application of the TSR-Canny approach with non-maximum suppression. Both defects are embedded in the same depth with the one of the nominal case, namely 1.5 mm under the upper surface and the SNR has been set to 10 dB. It appears that the applied approach yields overall satisfactory results for both cases.

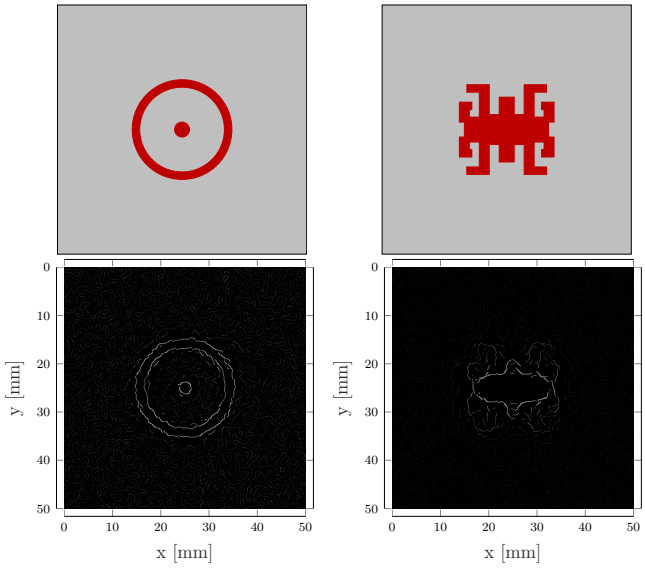

Figure 24: Defect geometries in the (x, y)-plane and the corresponding edge-detection results after application of the TSR-Canny approach. *Left column:* A disc of radius 1.5 mm included in a ring of internal radius 8.5 mm and external radius 10 mm. *Right column:* A complex shape of dimensions 20×18 mm.

5. Discussion

The TSR method has been combined with the Canny algorithm for the detection and the dimensioning of delamination defects in thermograms obtained using pulsed thermography. In this combined approach TSR is used for compression and denoising the raw signals, and the thus proceeded images are passed to the Canny algorithm. It is interesting to note the partial spatial denoising of the images (beside the temporal filtering) achieved by the TSR, which contributes to a beneficial improvement to the overall processing thus enhancing the performance of the Canny algorithm.

TSR has been also used as an acceleration technique for the simulation of the heat propagation problem, in the sense that the temperature field needs to be calculated at a limited number of time instances, used for the polynomial fitting when the TSR approximation is computed.

Combined with a fast semi-analytical solution based on the TREE approach, TSR provides a powerful tool.

This work is restricted to the characterisation of delamination defects in homogeneous and isotropic media with the thermal excitation being applied upon one of the piece interfaces. Volumetric heat production via ultrasonic of eddy current excitation [47, 48] are of great practical interest as well, and work is under way in order to extend the herein developed approach in order to treat such kind of inspection scenarios as well.

6. References

References

[1] X. Maldague, Introduction to NDT by active infrared thermography, Mater. Eval. 60 (9) (2002) 1060–1073.

[2] M. A. Omar, Y. Zhou, A quantitative review of three flash thermography processing routines, Infrared Phys. Technol. 51 (4) (2008) 300–306. doi:10.1016/j.infrared.2007.09.006.

[3] T. Li, D. P. Almond, D. S. Rees, Crack imaging by scanning pulsed laser spot thermography, NDT & E Int. 44 (2) (2011) 216–225. doi:10.1016/j.ndteint.2010.08.006.

[4] S. Burrows, S. Dixon, S. Pickering, T. Li, D. Almond, Thermographic detection of surface breaking defects using a scanning laser source, NDT & E Int. 44 (7) (2011) 589–596. doi:10.1016/j.ndteint.2011.06.001.

[5] X. Maldague, F. Galmiche, A. Ziadi, Advances in pulsed phase thermography, Infrared Phys. Technol. 43 (3-5) (2002) 175–181.

[6] V. Feuillet, L. Ibos, M. Fois, J. Dumoulin, Y. Candau, Defect detection and characterization in composite materials using square pulse thermography coupled with singular value decomposition analysis and thermal quadrupole modeling, NDT & E Int. 51 (2012) 58–67. doi:10.1016/j.ndteint.2012.06.003.

[7] A. A. Badghaish, D. C. Fleming, Non-destructive inspection of composites using step heating thermography, J. Compos. Mater. 42 (13) (2008) 1337–1357. doi:10.1177/0021998308092202.

[8] X. Maldague, Theory and Practice of Infrared Technology for Nondestructive Testing, Wiley, 2001.

[9] T. Sakagami, S. Kubo, Applications of pulse heating thermography and lock-in thermography to quantitative nondestructive evaluations, Infrared Phys. Technol. 43 (3-5) (2002) 211–218. doi:10.1016/S1350-4495(02)00141-X.

[10] X. Maldague, S. Marinetti, Pulse phase infrared thermography, J. Appl. Phys. 79 (5) (1996) 2694–2698. doi:10.1063/1.362662.

[11] N. Tabatabaei, A. Mandelis, Thermal-wave radar: A novel subsurface imaging modality with extended depth-resolution dynamic range, Rev. Sci. Instrum 80 (3) (2009) 034902. doi:10.1063/1.3095560.

[12] S. M. Shepard, Reconstruction and enhancement of active thermographic image sequences, Opt. Eng. 42 (5) (2003) 1337. doi:10.1117/1.1566969.

[13] D. L. Balageas, J. M. Roche, F. H. Leroy, W. M. Liu, A. M. Gorbach, The thermographic signal reconstruction method: A powerful tool for the enhancement of transient thermographic images, Biosybern. Biomed. Eng. 35 (1) (2015) 1–9. doi:10.1016/j.bbe.2014.07.002.

[14] N. Rajic, Principal component thermography for flaw contrast enhancement and flaw depth characterisation in composite structures, Compos. Struct. 58 (4) (2002) 521–528. doi:10.1016/S0263-8223(02)00161-7.

[15] F. Wang, Y.-H. Wang, W. Peng, J.-Q. Ji, J.-Y. Liu, P. Xiao, Y. Wang, Independent component analysis enhanced pulse thermography for high silicon oxygen phenolic resin (HSOPR) sheet with subsurface defects, Infrared Phys. Technol. 92 (2018) 345–349. doi:10.1016/j.infrared.2018.06.027.

[16] L. Cheng, B. Gao, G. Y. Tian, W. L. Woo, G. Berthiau, Impact Damage Detection and Identification Using Eddy Current Pulsed Thermography Through Integration of PCA and ICA, IEEE Sensors J. 14 (5) (2014) 1655–1663. doi:10.1109/JSEN.2014.2301168.

[17] R. Shrestha, Y. Chung, W. Kim, Wavelet transform applied to lock-in thermographic data for detection of inclusions in composite structures: Simulation and experimental studies, Infrared Phys. Technol. 96 (2019) 98–112. doi:10.1016/j.infrared.2018.11.008.

[18] B. Gao, A. Yin, G. Tian, W. Woo, Thermography spatial-transient-stage mathematical tensor construction and material property variation track, Int. J. Heat Mass Tran. 85 (2014) 112–122. doi:10.1016/j.ijthermalsci.2014.06.018.

[19] T. Liang, W. Ren, G. Y. Tian, M. Elradi, Y. Gao, Low energy impact damage detection in CFRP using eddy current pulsed thermography, Compos. Struct. 143 (2016) 352–361. doi:10.1016/j.compstruct.2016.02.039.

[20] Y. Laib dit Leksir, M. Mansour, A. Moussaoui, Localization of thermal anomalies in electrical equipment using Infrared Thermography and support vector machine, Infrared Phys. Technol. 89 (2018) 120–128. doi:10.1016/j.infrared.2017.12.015.

[21] B. Gao, W. L. Woo, Y. He, G. Y. Tian, Unsupervised Sparse Pattern Diagnostic of Defects With Inductive Thermography Imaging System, IEEE Trans. Ind. Informat. 12 (1) (2016) 371–383. doi:10.1109/TII.2015.2492925.

[22] D. P. Almond, S. K. Lau, Defect sizing by transient thermography. I. An analytical treatment, J. Phys. D: Appl. Phys. 27 (5) (1994) 1063–1069. doi:10.1088/0022-3727/27/5/027.

[23] S. Lugin, U. Netzelmann, A defect shape reconstruction algorithm for pulsed thermography, NDT & E Int. 40 (3) (2007) 220–228. doi:10.1016/j.ndteint.2006.11.001.

[24] J. Canny, A computational approach to edge detection, IEEE Trans. Pattern Anal. Mach. Intell. PAMI-8 (6) (1986) 679–698. doi:10.1109/TPAMI.1986.4767851.

[25] Alaknanda, R. S. Anand, P. Kumar, Flaw detection in radiographic weld images using morphological approach, NDT & E Int. 39 (1) (2006) 29–33. doi:10.1016/j.ndteint.2005.05.005.

[26] B. Yan, Y. Li, S. Ren, I. M. Zainal Abidin, Z. Chen, Y. Wang, Recognition and evaluation of corrosion profile via pulse-modulation eddy current inspection in conjunction with improved Canny algorithm, NDT & E Int. 106 (May) (2019) 18–28. doi:10.1016/j.ndteint.2019.05.007.

[27] F. C. Sham, N. Chen, L. Long, Surface crack detection by flash thermography on concrete surface, Insight: Non-Destructive Testing and Condition Monitoring 50 (5) (2008) 240–243. doi:10.1784/insi.2008.50.5.240.

[28] D. Maillet, S. André, J. C. Batsale, A. Degiovanni, C. Moyne, Thermal quadrupoles: soving the heat equation through integral transforms, 1st Edition, John Willey & Sons, Inc., 2000.

[29] O. Fudym, B. Ladevie, J.-C. Batsale, A seminumerical approach for heat diffusion in heterogeneous media: one extension of the analytical quadrupole method, Infrared Phys. Technol. 42 (4) (2002) 325–348. doi:ff10.1080/10407790190053978.

[30] O. Fudym, J.-C. Batsale, D. Lecomte, Heat diffusion at the boundary of stratified media: Homogenized temperature field and thermal constriction, Int. J. Heat Mass Tran. 47 (10) (2004) 2437 – 2447. doi:10.1016/j.ijheatmasstransfer.2003.11.014.

[31] T. P. Theodoulidis, E. E. Kriezis, Eddy Current Canonical Problems (with applications to nondestructive evaluation), Tech Science Press, Forsyth GA, 2006.

[32] T. Theodoulidis, J. R. Bowler, Interaction of an eddy-current coil with a right-angled conductive wedge, IEEE Trans. Magn. 46 (4) (2010) 1034–1042. doi:10.1109/TMAG.2009.2036724.

[33] A. Skarlatos, T. Theodoulidis, Semi-analytical calculation of the low-frequency electromagnetic scattering from a near-surface spherical inclusion in a conducting half-space, Proc. R. Soc. London, Ser. A 470 (2170) (Jun. 2014). doi:10.1098/rspa.2014.0269.

[34] A. Skarlatos, T. Theodoulidis, Calculation of the eddy-current flow around a cylindrical through-hole in a finite-thickness plate, IEEE Trans. Magn. 51 (9) (2015) 6201507. doi:10.1109/TMAG.2015.2426676.

[35] P. Vafeas, A. Skarlatos, T. Theodoulidis, D. Lesselier, Semi–analytical method for the identification of inclusions by air–cored coil interaction in ferromagnetic media, Math. Method. Appl. Sci. 41 (16) (2018) 6422–6442. doi:10.1002/mma.5168.

[36] J. R. Bowler, T. Theodoulidis, N. Poulakis, Eddy current probe signals due to a crack at a right-angled corner, IEEE Trans. Magn. 48 (12) (2012) 4735–4746. doi:10.1109/TMAG.2012.2203918.

[37] K. Pipis, A. Skarlatos, T. Theodoros, D. Lesselier, ECT-signal calculation of cracks near fastener holes using an integral equation formalism with dedicated Green's kernel, IEEE Trans. Magn. 52 (4) (2016) 6200608. doi:10.1109/TMAG.2015.2496189.

[38] A. Ratsakou, C. Reboud, A. Skarlatos, D. Lesselier, Model based characterisation of delamination by means of thermographic inspection, J. Phys. Conf. Ser. 1476 (2020) 012005. doi:10.1088/1742-6596/1476/1/012005.

[39] H. Stehfest, Algorithm 368. Numerical inversion of the Laplace transforms, ACM 13 (1) (1970) 47–49.

[40] H. Stehfest, Remark on algorithm 368. Numerical inversion of the Laplace transforms, ACM 13 (10) (1970) 624.

[41] D. P. Gaver, Observing stochastic process, and approximate transform inversion, Oper. Res. 14 (3) (1966) 444–459.

[42] S. M. Shepard, Advances in pulsed thermography, in: A. E. Rozlosnik, R. B. Dinwiddie (Eds.), Thermosense XXIII, Vol. 4360, International Society for Optics and Photonics, SPIE, 2001, pp. 511 – 515. doi:10.1117/12.421032.

[43] N. Otsu, A threshold selection method from gray-level histograms, IEEE Trans. Syst., Man, Cybern. 9 (1) (1979) 62–66. doi:10.1109/TSMC.1979.4310076.

[44] D. Sen, S. K. Pal, Gradient histogram: Thresholding in a region of interest for edge detection, Image Vision Comput. 28 (4) (2010) 677–695. doi:10.1016/j.imavis.2009.10.010.

[45] A. S. Abutaleb, Automatic thresholding of gray-level pictures using two-dimensional entropy, Comput. Gr. Image Process. 47 (1) (1989) 22–32. doi:10.1016/0734-189X(89)90051-0.

[46] R. Medina-Carnicer, R. Muñoz-Salinas, E. Yeguas-Bolivar, L. Diaz-Mas, A novel method to look for the hysteresis thresholds for the Canny edge detector, Pattern Recogn. 44 (6) (2011) 1201–1211. doi:10.1016/j.patcog.2010.12.008.

[47] A. Ratsakou, C. Reboud, A. Skarlatos, D. Lesselier, Fast models dedicated to simulation of eddy current thermography, in: D. Lesselier, C. Reboud (Eds.), Electromagnetic Nondestructive Evaluation (XXI), Vol. 43 of Studies in Applied Electromagnetics and Mechanics, IOS Press, Nieuwe Hemweg 6B, 1013 BG Amsterdam, Netherlands, 2018, pp. 175–182. doi:10.3233/978-1-61499-836-5-175.

[48] N. Siakavellas, The influence of the heating rate and thermal energy on crack detection by eddy current thermography, J. Nondestr. Eval. 35 (2) (2016). doi:10.1007/s10921-016-0337-9.